# Journal of Materials Chemistry A

Accepted Manuscript


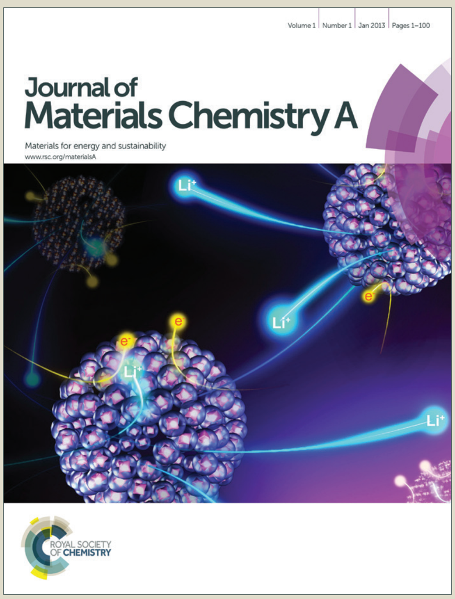

# Monodispersed nickel phosphide nanocrystals with different phases: synthesis, characterization and electrocatalytic properties for hydrogen evolution

*Yuan Pan, Yanru Liu, Jinchong Zhao, Kang Yang, Jilei Liang, Dandan Liu, Wenhui Hu, Dapeng Liu, Yunqi Liu*, Chenguang Liu*

*State Key Laboratory of Heavy Oil Processing, Key Laboratory of Catalysis, China National Petroleum Corporation (CNPC), China University of Petroleum, 66 West Changjiang Road, Qingdao, Shandong 266580, P. R. China*

* Corresponding author. E-mail address: liuyq@upc.edu.cn.

Tel.: +86-532-86981861.

**Abstract**

Monodispersed nickel phosphide nanocrystals (NCs) with different phases ($Ni_{12}P_5$, $Ni_2P$ and $Ni_5P_4$) were synthesized via the thermal decomposition approach using nickel acetylacetonate as nickel source, trioctylphosphine as phosphorus source and oleylamine in 1-octadecene as reductant. The phases of the as-synthesized nickel phosphide NCs could easily be controlled by changing the P:Ni precursor ratio. The structure and morphology of the as-synthesized nickel phosphide NCs were characterized by X-ray diffraction (XRD), transmission electron microscopy (TEM), energy dispersive X-ray analysis (EDX), X-ray photoelectron spectroscopy (XPS), Fourier transform infrared (FT-IR) and $N_2$ adsorption-desorption. A formation mechanism of the as-synthesized nickel phosphide NCs was proposed. We further studied the influence of the phase of the nickel phosphide NCs on the electrocatalytic properties for the hydrogen evolution reaction (HER). All phases showed good catalytic properties, and the $Ni_5P_4$ NCs with solid structure exhibited higher catalytic activity than the $Ni_{12}P_5$ and $Ni_2P$ NCs. This superior catalytic activity is attributed to the higher positive charge of Ni and a stronger ensemble effect of P in $Ni_5P_4$ NCs. This study demonstrates that the crystalline phase is important for effecting the electrocatalytic properties.

**Keywords:** nickel phosphide; phase-controlled synthesis; electrocatalytic properties; hydrogen evolution reaction.

## 1. Introduction

Nowadays, more and more attention is being paid to the production of hydrogen due to the increase of global demand for energy and the aggravation of environmental problems by burning fossil fuels[1]. The emission of $SO_x$ and $CO_x$ in fuels combustion process is leads to the formation of acid rain, global warming and air pollution[2]. In addition, hydrogen also has been intensively used in a variety of industrial fields, such as petroleum refining and ammonia synthesis[3]. Therefore, developing a more convenient, efficient and environmental friendly approach to produce hydrogen is highly desired. Electrolysis of water is the most promising technology for hydrogen production[4]. Up to now, noble metals such as Pt have been used as the most effective electrocatalyst for the hydrogen evolution reaction (HER)[5]. However, the large scale application of noble metals is limited due to the high price and resource scarcity[6]. Therefore, more and more research is focused on the development of non-noble metal electrocatalysts with low cost and high abundance. Over the past years, Mo-based non-noble metal materials such as $MoS_2$[7], MoB[8] and $Mo_2C$[9] have been identified as active HER catalysts in both acidic and alkaline solutions. In addition, Ni-based alloys such as Ni-Mo[10], Ni-Mo-Zn[11] and Ni-Fe[12] also exhibited high activity for the HER. Recently, transition metal phosphide has attracted considerable attention as electrocatalyst with high activity and stability. For example, Xiao et al.[13] demonstrated that molybdenum phosphide exhibited high electrocatalytic performance in both acidic and alkaline conditions. Schaak et al.[14] reported that nanostructured nickel phosphide ($Ni_2P$) with a high accessible surface area and a high density of exposed (001) facets could be used as a potential HER catalyst to replace noble metal. Huang et al.[15] reported that $Ni_{12}P_5$ nanoparticles (NPs) also can be used as efficient catalyst for hydrogen generation via electrolysis and photoelectrolysis. In general, nickel phosphide exist in a variety of phases, such as $Ni_3P$, $Ni_2P$, $Ni_5P_2$, $Ni_{12}P_5$ and $Ni_5P_4$. Many studies also suggested that the phase and morphology of nanocrystals (NCs) played an important role in the catalytic properties[16]. Therefore, research on the phase-dependent electrocatalytic properties of nickel phosphide for the HER is very important, but relevant reports are scarce.

In recent years, various methods have been attempted to synthesize monodispersed nickel phosphide NCs, such as thermal decomposition of organometallic precursors[26], solvothermal synthesis[17], chemical vapor deposition[18] and microwave synthesis[19]. Among these methods, the thermal decomposition of organometallic precursor has the advantage that the reaction can be easily achieved, and that the phase, size and morphology of nickel phosphide can be controlled by changing the reaction conditions. For example, Muthuswamy et al.[20] reported that $Ni_{12}P_5$ and $Ni_2P$ NPs with hollow and solid morphology could be synthesized by changing the P:Ni precursor ratio. Savithra et al.[21] reported that the size of $Ni_2P$ NPs could be controlled by varying the quantity of oleylamine. Although the synthesis of nickel phosphide NPs has been achieved in recent studies, reports are rare on the synthesis of nickel phosphide NCs with different phases ($Ni_{12}P_5$, $Ni_2P$ and $Ni_5P_4$) and morphologies (hollow and solid structure), and the formation mechanism of nickel phosphide NCs with different phases and morphologies was not clearly explained.

In this work, we report for the first time the phase-controlled synthesis of monodispersed nickel phosphide NCs via the thermal decomposition approach using nickel acetylacetonate as nickel source, trioctylphosphine as phosphorus source and oleylamine in 1-octadecene as reductant. The phase-controlled synthesis was realized by changing the molar ratio of P:Ni precursor. The structure and morphology of the as-synthesized nickel phosphide NCs were characterized by X-ray diffraction (XRD), transmission electron microscopy (TEM), energy dispersive X-ray analysis (EDX), X-ray photoelectron spectroscopy (XPS) and Fourier transform infrared (FT-IR). The possible formation mechanism of nickel phosphide NCs was proposed in detail. Furthermore, the phase influences of the nickel phosphide NCs on electrocatalytic properties for HER in 0.5 M $H_2SO_4$ were systematically investigated. The results showed that all phases of the as-synthesized nickel phosphide NCs have good catalytic properties, and that the $Ni_5P_4$ NCs with solid structure exhibited higher catalytic activity than the $Ni_{12}P_5$ and $Ni_2P$ NCs.

## 2. Experimental

### *2.1 Materials*

Nickel(II) acetylacetonate ($Ni(acac)_2$, 95%), trioctylphosphine (TOP, 90%), oleylamine (OAm, 95%) and 1-octadecene (ODE, 95%) were obtained from Aladdin Chemistry Co. Ltd. Hexane (≥99.5%), ethanol (≥99.7%), and sulfuric acid ($H_2SO_4$, 98%) were obtained from Sinopharm Chemical Reagent Co., Ltd. Nafion solution (5% in a mixture of lower aliphatic alcohols and water) was purchased from Sigma-Aldrich. All chemicals were used as received without further purification. All reactions were carried out under argon atmosphere using standard air-free techniques.

*2.2 Synthesis of $Ni_{12}P_5$, $Ni_2P$ and $Ni_5P_4$ NCs*

In a typical reaction, $Ni(acac)_2$, OAm (7 mL, 21.3 mmol) and ODE (4.5 mL, 14.1 mmol) were placed in a four-neck flask and stirred magnetically under a flow of argon. The mixture was raised to 120 $^{o}$C with a heating rate of 10 °C·min$^{-1}$ and kept at this temperature for 30 min to remove moisture and dissolved oxygen. After TOP was quickly injected into the solution, the mixture was rapidly heated to 320 $^{o}$C and maintained for 2 h. The molar ratio of the P:Ni precursor was typically kept at 0.65. The color of the solution changed from blue, green, dark green to black. After cooling to room temperature, the black precipitate was obtained from the solution by adding excess ethanol and separated by centrifugation (4000 rpm, 10 min), then the black precipitate was washed with the mixture of hexane and ethanol. This procedure was carried out at least three times to remove excess surfactant and organic solvent. Finally, $Ni_{12}P_5$ NCs were obtained by drying in vacuum at 60 $^{o}$C for 24 h. Without changing other synthetic conditions, $Ni_2P$ NCs were obtained by increasing the molar ratio of P:Ni precursor to 2.18. $Ni_5P_4$ NCs were obtained by further increasing the molar ratio of P:Ni precursor to 8.75. When the molar ratio of P:Ni precursor was between 0.65 and 2.18, the products were a mixture of $Ni_{12}P_5$ and $Ni_2P$ crystalline phases. When the molar ratio of P:Ni precursor was between 2.18 and 8.75, the products were a mixture of $Ni_2P$ and $Ni_5P_4$ crystalline phases.

*2.3 Characterization*

XRD was performed on a panalytical X'pert PROX-ray diffractometer with Cu Kα monochromatized radiation ($\lambda$= 1.54 Å) and operated at 45 kV and 40 mA. The scan rate was 8° $min^{-1}$ and the 2 $\theta$ scan range was from 20° to 90°. TEM was performed on a JEM-2100 UHR microscope (JEOL, Japan) at an accelerating voltage of 200 kV. EDX was attached to the TEM system. The sample for TEM analysis was prepared by sonicating in hexane and depositing a drop on an amorphous carbon coated copper grid, which was allowed to slowly dry at ambient condition. XPS was performed on a VG ESCALABMK II spectrometer using an Al $K_\alpha$ (1486.6 eV) photon source. FT-IR spectra were collected on a Nexus spectrometer (Nicolet, USA) in the range of 4000 ~ 400 $cm^{-1}$ with 32 scans and the samples were prepared as KBr pellets. $N_2$ adsorption-desorption experiments were carried out on a ChemBET 3000 (Quantachrome, USA) instrument.

*2.4 Electrochemical measurements*

5 mg of the samples and 80 μL Nafion solution (5 wt.%) were dispersed in 1 mL ethanol and sonicated for 30 min to form a slurry. Then 5 μL of the slurry was loaded onto the surface of a glassy carbon electrode (GCE, 4 mm in diameter), and the GCE was dried at room temperature. The electrochemical measurement was carried out using a CHI660D potentiostat (CH Instruments, China) in a standard three-electrode setup. A saturated calomel electrode (SCE) was used as reference electrode and a Pt electrode as counter electrode. The electrocatalytic activity of the sample towards the HER was examined by obtaining polarization curves using linear sweep voltammetry (LSV) with a scan rate of 5 $mV \cdot s^{-1}$ at room temperature in 0.5 M $H_2SO_4$ solutions. A durability test was carried out by cyclic voltammetry (CV) scanning 500 cycles with a

scan rate of 100 mV·s$^{-1}$ in 0.5 M $H_2SO_4$. Electrochemical impedance spectroscopy (EIS) measurements were carried out in the frequency range of 100 kHz ~ 0.1 Hz with an overpotential of 200 mV. All the electrochemical data are presented without iR compensation. All the potentials reported in our work are versus the reversible hydrogen electrode (RHE). In 0.5 M $H_2SO_4$, E(RHE) = E(SCE) + (0.222 + 0.059 pH).

## 3. Results and discussion

### *3.1 Characterization of nickel phosphide NCs*

#### *3.1.1 XRD*

In our experiments, the molar ratio of the P:Ni precursor was found to be a key factor, which affects the phase structure of the nickel phosphide NCs. The crystalline phase structure and the purity of the as-synthesized nickel phosphide NCs at different P:Ni precursor molar ratios were characterized by XRD (Fig. 1). A phase transformation process occurs with increasing of the P:Ni precursor ratio. When the P:Ni precursor ratio was 0.65, the product was $Ni_{12}P_5$, and all the diffraction peaks matched well with the tetragonal structure of $Ni_{12}P_5$ (PDF # 03-065-1623). The diffraction peaks at 32.7°, 35.8°, 38.3°, 41.7°, 44.5°, 47.1°, 48.9°, 54.1°, 56.1°, 68.5°, 74.3°, 79.6° and 88.8° are attributed to the (310), (301), (112), (400), (330), (240), (312), (510), (501), (161), (004), (262) and (552) crystal phases, and no extraneous peaks exist, which indicates that the as-synthesized $Ni_{12}P_5$ is a pure phase. When the P:Ni precursor ratio was increased to 1.1, the product was a mixture of the tetragonal $Ni_{12}P_5$ and hexagonal $Ni_2P$ phases (Fig. 1b). Upon further increasing the P:Ni precursor ratio to 2.18, pure $Ni_2P$ phase was obtained (Fig. 1c). All diffraction peaks matched well with the hexagonal structure of $Ni_2P$ (PDF # 03-065-3544). The diffraction peaks at 40.8°, 44.7°, 47.5°, 54.4°, 66.4°, 72.6°, 75.0°, 80.5° and 88.9° are attributed to the (111), (201), (210), (300), (310), (311), (400), (401) and (321) crystal phases, and no extraneous peaks was observed. Further increasing the P:Ni precursor ratio to 5.45 and 7, the product was a mixture of hexagonal $Ni_2P$ and hexagonal $Ni_5P_4$ phases (Fig. 1d ~ e). Furthermore, when the P:Ni precursor ratio reached 8.75, the pure $Ni_5P_4$ phase was obtained (Fig. 1f). All diffraction peaks matched well with the hexagonal structure of $Ni_5P_4$ (PDF # 03-065-2075). The diffraction peaks at 28.8°, 30.4°, 31.5°, 34.7°, 36.1°, 40.6°, 41.4°, 46.3°, 47.0°, 47.9°, 49.9°, 53.1°, 54.1°, 75.1°, 77.9° and 85.8° are attributed to the (103), (200), (201), (202), (104), (210), (211), (300), (301), (213), (006), (303), (220), (323), (307) and (330) crystal phases, and no extraneous peaks existed. Thus, it can be concluded that increasing the P:Ni precursor ratio from 0.65 to 8.75 leads to a phase transformation from tetragonal $Ni_{12}P_5$ to hexagonal $Ni_5P_4$.

*3.1.2 TEM and EDX*

The morphologies of the as-synthesized $Ni_{12}P_5$, $Ni_2P$ and $Ni_5P_4$ NCs were characterized by TEM. Fig. 2a ~ b show the morphology images of the as-synthesized $Ni_{12}P_5$ NCs. The as-synthesized $Ni_{12}P_5$ NCs exhibited hollow structure with an average particle size of 17.55 ± 2.25 nm (insert in Fig. 2a). The HRTEM image (Fig. 2b) reveals that the fringe spacings are about 2.1 Å and 1.9Å, corresponding to the (400) and (240) lattice planes of tetragonal $Ni_{12}P_5$. The ED pattern (insert in Fig. 2b) indicates that the major diffraction rings match well with the tetragonal structure of

$Ni_{12}P_5$, which further confirms the crystal structure of $Ni_{12}P_5$. Fig. 2c ~ d show the morphology images of the as-synthesized $Ni_2P$ NCs. Similar as the $Ni_{12}P_5$ NCs, the as-synthesized $Ni_2P$ NCs also exhibited hollow structure, but the size was decreased with an average particle size of 9.19 ± 1.16 nm (insert in Fig. 2c). However, some solid structure can also be observed, this indicates that the morphology of the nickel phosphide NCs can be changed by increasing the ratio of the P:Ni precursor. The HRTEM image (Fig. 2d) reveals that the fringe spacing is about 2.21 Å, corresponding to the (111) lattice plane of hexagonal $Ni_2P$. The ED pattern (inserted in Fig. 2d) indicates that the major diffraction rings match well with the hexagonal structure of $Ni_2P$, which further confirms the crystal structure of $Ni_2P$. Fig. 2e shows the morphology image of the as-synthesized $Ni_5P_4$ NCs. Big solid spheres were obtained with an average particle size of 600 nm. The ED pattern (insert in Fig. 2e) indicates that the as-synthesized $Ni_5P_4$ NCs have good crystallinity. In addition, the chemical compositions of $Ni_{12}P_5$, $Ni_2P$ and $Ni_5P_4$ were further characterized by EDX spectra. Fig. S1 show the EDX spectra of $Ni_{12}P_5$, $Ni_2P$ and $Ni_5P_4$ NCs, respectively. The measured atomic ratio of Ni:P are 2.25:1, 1.87:1 and 1.33:1, which are very close to the stoichiometric ratio of 2.4:1, 2:1 and 1.25:1 in $Ni_{12}P_5$, $Ni_2P$ and $Ni_5P_4$, respectively.

*3.1.3 XPS*

The chemical states of Ni and P in the as-synthesized nickel phosphide NCs were characterized by XPS. Fig. 3a ~ b, c ~ d and e ~ f show the XPS spectra of the Ni 2p and P 2p regions for $Ni_{12}P_5$, $Ni_2P$ and $Ni_5P_4$, respectively. Fig. 3a shows three peaks around 852.6, 855.4 eV and 860.3 eV for Ni $2p_{3/2}$ energy level, corresponding to $Ni^{\delta+}$ in $Ni_{12}P_5$, oxidized Ni species and the satellite of Ni $2p_{3/2}$ peak[15]. Three peaks are observed at 869.5, 873.8 and 878.8 eV for the Ni $2p_{1/2}$ energy level, which are assigned to $Ni^{\delta+}$ in $Ni_{12}P_5$, oxidized Ni species and the satellite of Ni $2p_{1/2}$ peak, respectively. The $Ni_2P$ (Fig. 3c) and $Ni_5P_4$ (Fig. 3e) NCs have similar Ni $2p_{3/2}$ and Ni $2p_{1/2}$ energy level with $Ni_{12}P_5$ NCs. In addition, the peaks at 852.6 eV, 852.8 eV and 830.0 eV in $Ni_{12}P_5$, $Ni_2P$ and $Ni_5P_4$ are very close to that of zero valence state Ni, which indicates that the Ni species in $Ni_{12}P_5$, $Ni_2P$ and $Ni_5P_4$ have a very small positive charge ($Ni^{\delta+}$)[15, 27], and that the value of δ is in the order: $\delta$ ($Ni_{12}P_5$) < $\delta$ ($Ni_2P$) < $\delta$ ($Ni_5P_4$). For the P 2p region, peaks at 129.5 (Fig. 3b), 129.6 (Fig. 3d) and 129.4 eV (Fig. 3f) can be assigned to P in $Ni_{12}P_5$, $Ni_2P$ and $Ni_5P_4$ NCs, and these binding energy value are less than that of elemental P (130.2 eV), which indicates that the P species in $Ni_{12}P_5$, $Ni_2P$ and $Ni_5P_4$ have a very small negative charge ($P^{\delta-}$)[15, 27]. These results suggest that there is an electron transfer from Ni to P in all nickel phosphide NCs phases. Furthermore, three peaks are observed at 133.9 (Fig. 3b), 133.2 (Fig. 3d) and 133.4 eV (Fig. 3f) in the P 2p energy region, which can be assigned to small amounts of oxidized P species formed on the surface of nickel phosphide because the samples ware exposed to air[28]. Moreover, the calculated atomic ratios of Ni:P from the XPS spectra are 2.45:1, 1.85:1 and 1.05:1, which are very close to the stoichiometric ratio of 2.4:1, 2:1 and 1.25:1 in $Ni_{12}P_5$, $Ni_2P$ and $Ni_5P_4$, respectively. The XPS depth profiling analysis (Fig. S2) indicate that the change of content of both Ni and P elements from $Ni_{12}P_5$, $Ni_2P$ and $Ni_5P_4$ NCs are very small during $Ar^+$ etching, suggesting homogeneous distribution of both Ni and P elements inside the NPs[46].

*3.1.4 FTIR*

The surface states of the as-synthesized nickel phosphide NCs before and after annealing were characterized by FT-IR analysis. As shown in Fig. 4I, the absorption peaks at 2926 and 2855 $cm^{-1}$ are due to the stretching vibration of C-H in methyl and methylene. The absorption peak at 1630 $cm^{-1}$ is attributed to the stretching vibration of C=C in OAm. The absorption peak at 1058 $cm^{-1}$ is attributed to the stretching vibration of C-P, which indicates the coordination of the TOP on the surface of the nickel phosphide NCs. These results are in agreement with our previous report[29]. The absorption peaks from 720 to 560 $cm^{-1}$ is attributed to the stretching vibration of long carbon chain. According to the results, TOP and OAm act as ligand coexisting on the surface of nickel phosphide. However, when the samples were heated at 450 °C in 5% $H_2$ / Ar for 30 min (Fig. 4II), these peaks disappeared, and no peaks be attributed to functional groups of organic components can be observed. This indicates that the organic ligands that capped the surface of the nickel phosphide were removed[15, 26a].

*3.1.5 Textural properties*

The textural properties (BET surface area, pore volume and pore size) of the as-synthesized nickel phosphide NCs with different phases are shown in Table 1. It can be observed that $Ni_{12}P_5$ NCs exhibit a lower BET surface area than the other phases, whereas $Ni_5P_4$ NCs have the highest surface area, which means more exposed active sites. Meanwhile, the pore volume and pore size decreased gradually with the phase transformation from $Ni_{12}P_5$ to $Ni_5P_4$. The $N_2$ adsorption-desorption isotherms and BJH pore-size distribution of the as-synthesized nickel phosphide NCs with different phases are shown in Fig. 5. The isotherms belong to type IV which is typical for mesoporous material.

*3.2 Possible formation mechanism*

The TEM results showed that the morphology of the nickel phosphide NCs can be controlled by changing the P:Ni precursor ratio. The formation of hollow $Ni_{12}P_5$ NCs can be explained via a nanoscale Kirkendall pathway[30]. OAm acted as the reductant to form nickel nanoclusters when the reaction temperature reached 200°C. TOP is a strong ligand, which can adsorb on the surface of nickel NPs and form Ni-TOP complexes[29]. When the reaction temperature reached 320°C, the P-C bonds broke and phosphorus atoms formed, which can diffuse into the nickel nanoclusters. However, the outward diffusion rate of nickel atoms is faster than the inward diffusion rate of phosphorus atoms at low P:Ni precursor ratio, which leads to the formation of hollow $Ni_{12}P_5$ NCs. Meanwhile, the increase of the P:Ni precursor ratio is favorable to the inward diffusion of phosphorus atoms, and both hollow and solid $Ni_2P$ NCs are obtained. When the P:Ni precursor ratio is further increased, different results can be observed. The product is comprised of $Ni_5P_4$ solid spheres with large size (about 600 nm). The formation of solid NPs is due to the diffusion of nickel and phosphorus atoms that reached a balanced state in all directions. However, the solid NPs are unstable in solution due to the high surface energy and intermolecular forces[31], which led to the rapid aggregation of $Ni_5P_4$ NPs and the formation of large size $Ni_5P_4$ solid spheres. The possible formation mechanism of the as-synthesized nickel phosphide

NCs with different phases and morphologies is summarized in Fig. 6.

*3.3 Phase-dependent electrocatalytic properties*

Generally, the crystalline phase is one of the most important factors which can dominate catalytic activity[32]. The HER catalytic activity of nickel phosphide NCs with different phases was evaluated by electrochemical experiments. Before the electrochemical measurements, the samples were annealed in flowing $H_2$ (5%) / Ar (95%) at 450 °C for 30 min to remove the organic ligands that capped the surface of the nickel phosphide NCs (as shown in part 3.1.4 ). The LSV curves of $Ni_{12}P_5$, $Ni_2P$ and $Ni_5P_4$ in 0.5 M $H_2SO_4$ with a slow scan rate of 5 $mV \cdot s^{-1}$ using a three-electrode setup with the same loading of 1.99 $mg \cdot cm^{-2}$ on GCE are shown in Fig. 7. The bare GCE exhibits small HER activity. The onset potentials for $Ni_{12}P_5$, $Ni_2P$ and $Ni_5P_4$ NCs were 80, 62 and 34 mV, respectively. Likewise, when the HER current density reached 10 $mA \cdot cm^{-2}$, the potentials were 208, 137 and 118 mV for $Ni_{12}P_5$, $Ni_2P$ and $Ni_5P_4$ NCs. These results demonstrate that nickel phosphide NCs with different phases have good electrocatalytic properties, and that the $Ni_5P_4$ NCs with solid structure exhibit the highest catalytic activity compared with $Ni_{12}P_5$ and $Ni_2P$ NCs. This superior HER activity can be attributed to the positive charge of Ni and the ensemble effect of P[15]. The small positive charge of Ni is beneficial to the HER. The XPS studies showed that $\delta$ ($Ni_{12}P_5$) < $\delta$ ($Ni_2P$) < $\delta$ ($Ni_5P_4$), which indicates that the catalytic activity of $Ni_5P_4$ NCs is better than that of the $Ni_{12}P_5$ and $Ni_2P$ NCs. In addition, the ensemble effect of P is beneficial for improving the catalytic activity by decreasing the number of exposed Ni active sites[33]. This is in accord with our experimented results, because the contents of P in three nickel phosphide NCs are $Ni_{12}P_5$ (29 at% P) < $Ni_2P$ (33 at% P) < $Ni_5P_4$ (44 at% P). In addition, Nicolet et al[39] reported that hydrogenase uses pendant bases proximate to the metal centers as active sites for hydrogen evolution.Wilson et al[40] thought that the metal complex HER catalyst also incorporates proton relays from pendant acid-base groups positioned close to the metal center where hydrogen evolution occurs. Sun group recent works have shown that transition metal phosphides (TMPs), including CoP[41], MoP[42], $Cu_3P$[43], $Ni_2P$[44], $NiP_2$[45] and FeP[46], exhibit high HER catalytic activity and feature a metal center ($\delta^+$) with a pendant base P ($\delta^-$ ) close to it. In our present study, the nickel phosphide NCs with different phases ($Ni_{12}P_5$, $Ni_2P$, $Ni_5P_4$) also features a metal center Ni ($\delta^+$) with a pendant base P ($\delta^-$ ) close to it. The Ni and P act as the hydride-acceptor and proton-acceptor center to facilitate the HER[47], and the P also could facilitate the formation of Ni-hydride for subsequent hydrogen evolution via electrochemical desorption[48]. Therefore, $Ni_{12}P_5$, $Ni_2P$ and $Ni_5P_4$ NCs adopt a similar catalytic mechanism with hydrogenase, metal complexes and TMP catalysts toward the HER. Moreover, $Ni_5P_4$ NCs are expected to offer more proton-acceptor centers and thus more active sites because of its P-rich nature[45]. That is why $Ni_5P_4$ NCs exhibit superior HER activity than $Ni_{12}P_5$ and $Ni_2P$ NCs. Furthermore, the surface area also significantly influence the electrochemical performances, the $Ni_5P_4$ NCs have the highest BET surface area (54.2 $m^2/g$), which means more exposed active sites and further improve the catalytic activity. Table S1 compares the HER activity of $Ni_{12}P_5$, $Ni_2P$ and $Ni_5P_4$ NCs with some reported transition metal phosphides, including

CoP NWs, CoP NSs, CoP NSs, amorphous MoP, bulk CoP, FeP NSs, $Ni_2P$ NPs, $Ni_{12}P_5$ NPs, $Ni_2P$/Ti, $NiP_2$ NS/CC, CoP/CNT, MoP-CA2 NPs, CoP NPs/CC, CoP/Ti, MoP/CF, $Cu_3P$ NW/CF, CoP/CC, CoP NTs, np-CoP NWs/Ti and FeP NA/Ti. The potentials for $Ni_5P_4$ NCs compare favorably to the behavior of other transition metal phosphides in acidic media.

The reaction mechanism of HER can be explained by Tafel analysis. Fig. 8 shows that the Tafel plots of $Ni_{12}P_5$, $Ni_2P$ and $Ni_5P_4$ NCs derived from the polarization curves fit well with the Tafel equation ($\eta$ = a + b log j, where b is the Tafel slope and j is the current density). The Tafel slopes for $Ni_{12}P_5$, $Ni_2P$ and $Ni_5P_4$ are 75, 49 and 42 $mV \cdot dec^{-1}$, which indicates that the HER rate of $Ni_5P_4$ is faster than that of the $Ni_{12}P_5$ and $Ni_2P$ with the increase of potential. The smaller Tafel slope of $Ni_5P_4$ NCs demonstrates that the catalytic performance is better than that of the $Ni_{12}P_5$ and $Ni_2P$ NCs. The exchange current density values of $Ni_{12}P_5$, $Ni_2P$ and $Ni_5P_4$ NCs were also obtained by applying the extrapolation method to the Tafel plots. As shown in Table S2, the $Ni_5P_4$ NCs display the largest exchange current density of 57.02 $\mu A \cdot cm^{-2}$, which indicates the best catalytic activity among all the tested samples. Generally, three possible reaction steps have been proposed for the HER in acidic solutions[34], commonly named the Volmer reaction: $H_3O^+ + e^- \rightarrow H_{ad} + H_2O$ (1), the Heyrovsky reaction: $H_3O^+ + e^- + H_{ad} \rightarrow H_2 + H_2O$ (2) and the Tafel reaction: $H_{ad} + H_{ad} \rightarrow H_2$ (3). When Eq. (1) is the rate determining step of the HER, the Tafel slope is 120 $mV \cdot dec^{-1}$. When Eq. (1) is fast and Eq. (2) or Eq. (3) are the rate determining step, the Tafel slope is 30 and 40 $mV \cdot dec^{-1}$[35]. In our studies, the observed Tafel slope of $Ni_{12}P_5$,

$Ni_2P$ and $Ni_5P_4$ NCs were 75, 49 and 42 mV·dec$^{-1}$, which indicates that the HER reaction took place via a fast Volmer step followed by a rate determining Heyrovsky step[4, 36].

Besides the catalytic activity, the stability is another important factor for evaluating a electrocatalyst[37]. The stability of $Ni_{12}P_5$, $Ni_2P$ and $Ni_5P_4$ NCs was tested using CVs measurements by scanning 500 cycles from -0.4 to 0.2 V vs. SCE with a scan rate of 100 mV·s$^{-1}$ in 0.5 M $H_2SO_4$, as shown in Fig. 9a. There are only slight losses of current density after 500 cycles for the three catalysts, which indicates that all phases of the nickel phosphide NCs have an excellent cycle life in acidic environment. It also can be observed that the current density loss of $Ni_{12}P_5$ NCs is larger than of the other two catalysts, and the $Ni_5P_4$ NCs show the smallest current density loss, which indicates that the $Ni_5P_4$ NCs exhibit the best stability. Furthermore, the time-dependent current density curve of the $Ni_{12}P_5$, $Ni_2P$ and $Ni_5P_4$ NCs under static overpotential of 150 mV (Fig. 9b) suggests that all phases of the as-synthesized nickel phosphide NCs maintain their catalytic activity for at least 30 000 s.

In addition, EIS experiments were carried out to get further insight into the HER process of $Ni_{12}P_5$, $Ni_2P$ and $Ni_5P_4$ NCs. The results are shown in Nyquist plots in Fig. 10. The $Ni_5P_4$ NCs have the smallest diameter and $Ni_{12}P_5$ NCs have the largest diameter, which further indicate that the $Ni_5P_4$ NCs show the smallest charge transfer resistance, and exhibit superior HER activity[38].

**4. Conclusions**

Monodispersed nickel phosphide NCs were successfully synthesized via the thermal decomposition approach using $Ni(acac)_2$ as nickel source, TOP as phosphorus source and OAm in ODE as reductant. The phase-controlled synthesis was achieved by changing the molar ratio of P:Ni precursor. Generally, a higher P:Ni precursor ratio (P:Ni = 8.75) is beneficial for forming the $Ni_5P_4$ phase with solid morphology, while a lower P:Ni precursor ratio (P:Ni = 0.65) is beneficial for forming the $Ni_{12}P_5$ phase with hollow morphology. When the molar ratio of P:Ni precursor was 2.18, $Ni_2P$ NCs were obtained. The formation of hollow $Ni_{12}P_5$ NCs could be explained via a nanoscale Kirkendall pathway, while the solid $Ni_5P_4$ NCs could be attributed to the rapid aggregation of nanoclusters. Electrochemical tests demonstrated that all phases of the as-synthesized nickel phosphide NCs showed good electrocatalytic properties, and the $Ni_5P_4$ NCs exhibited much better catalytic activity than the $Ni_{12}P_5$ and $Ni_2P$ NCs. This is attributed to the higher positive charge of Ni and a stronger ensemble effect of P in $Ni_5P_4$ NCs. This study shows that the crystalline phase is important for effecting the electrocatalytic properties.

**Acknowledgements**

This work was financially supported by the National Key Fundamental Research Development Project of China (973 Project No. 2010CB226905), the National Natural Science Foundation of China (Grants No. 21006128, 21176258, U1162203, 21301190), China University of Petroleum for Postgraduate Technology Innovation Project (Grants No. YCX2014033), the Specialized Research Fund for the Doctoral Program of Higher Education of China (Grant No. 20110133110002) and the Fundamental Research Funds for the Central Universities (Grant No. 14CX02005A).

We thank Professor R. Prins for helpful comments during the preparation of the manuscript.

**References**

1. B. Hinnemann, P. G. Moses, J. Bonde, K. P. Jørgensen, J. H. Nielsen, S. Horch, I. Chorkendorff, J. K. Nørskov, *J. Am. Chem. Soc*, 2005, **127**, 5308-5309.

2. M. Rahhal, A. Ghata, Y. Hourieh, *Pet. & Coal*, 2009, **51**, 150-159.

3. (a) J. D. Benck, Z. Chen, L. Y. Kuritzky, A. J. Forman, T. F. Jaramillo, ACS Catal, 2012, **2**, 1916-1923. (b) X. Xia, Z. Zheng, Y. Zhang, X. Zhao, C. Wang, *Int. J. Hydrogen Energ*, 2014, **39**, 9638-9650.

4. Z. Pu, Q. Liu, A. M. Asiri, A. Y. Obaid, X. Sun, *Electrochim. Acta*, 2014, **134**, 8-12.

5. (a) M. Daniel, X. Hu, *Energ. & Environ. Sci*, 2011, **4**, 3878-3888. (b) H. B. Gray, *Nat. Chem*, 2009, **1**, 7-7.

6. (a) M. Arenz, V. Stamenkovic, T. J. Schmidt, K. Wandelt, P. N. Ross, N. M. Markovic, *Surf. Sci*, 2002, **506**, 287-296. (b) B. Fang, J. H. Kim, J. S. Yu, *Electrochem. Commun*, 2008, **10**, 659-662.

7. D. Wang, Z. Pan, Z. Wu, Z. Wang, Z. Liu, *J. Power Sources*, 2014, **264**, 229-234.

8. V. Heron, X. Hu, *Angew. Chem*, 2012, **124**, 12875-12878.

9. W. F. Chen, C. H. Wang, K. Sasaki, N. Marinkovic, W. Xu, J. T. Muckerman, Y. Zhu, R. R. Adzic, *Energ. & Environ. Sci*, 2013, **6**, 943-951.

10. D. E. Brown, M. N. Mahmood, M. C. M. Man, A. K. Turner, *Electrochim. Acta*, 1984, **29**, 1551-1556.

11. D. G. Nocera, *Accounts Chem. Res*, 2012, **45**, 767-776.

12. I. A. Raj, K. I. Vasu, *J. Appl. Electrochem*, 1990, **20**, 32-38.

13. P. Xiao, M. A. Sk, L. Thia, X. Ge, R. J. Lim, J. Y. Wang, K. H. Lim, X. Wang, *Energ. & Environ. Sci*, 2014, **7**, 2624-2629.

14. E. J. Popczun, J. R. McKone, C. G. Read, A. J. Biacchi, A. M. Wiltrout , N. S. Lewis, & R. E. Schaak, *J. Am. Chem. Soc*, 2013, **135**, 9267-9270.

15. Z. Huang, Z. Chen, Z. Chen, C. Lv, H. Meng, C. Zhang, *ACS Nano*, 2014, **8**, 8121-8129.

16. H. Yang, L. Liu, H. Liang, J. Wei, Y. Yang, *CrystEngComm*, 2011, **13**, 5011-5016.

17. S. L. Liu, X. Z. Liu, L. Q. Xu, Y. T. Qian, *J. Cryst. Growth*, 2007, **304**, 430-434.

18. A. Panneerselvam, M. A. Malik, M. Afzaal, P. O'Brien, M. Helliwell, *J. Am. Chem. Soc*, 2008, **130**, 2420-2421.

19. X. Hu, J. C. Yu, *Chem. Mater*, 2008, **20**, 6743-6749.

20. E. Muthuswamy, G. H. L. Savithra, L. B. Stephanie, *ACS Nano*, 2011, **5**, 2402-2411.

21. G. H. Layan Savithra, E. Muthuswamy, R. H. Bowker, B. A. Carrillo, M. E. Bussell, S. L. Brock, *Chem. Mater*, 2013, **25**, 825-833.

22. P. Jiang, Q. Liu, C. Ge, W. Cui, Z. Pu, A. M. Asiri, X. Sun, *J. Mater. Chem. A*, 2014, **2**, 14634-14640.

23. J. M. McEnaney, J. C. Crompton, J. F. Callejas, E. J. Popczun, A. J. Biacchi, N. S. Lewis, R. E. Schaak, *Chem. Mater*, 2014, **26**, 4826-4831.

24. Y. Xu, R. Wu, J. Zhang, Y. Shi, B. Zhang, *Chem. Commun*, 2013, **49**, 6656-6658.

25. L. Feng, H. Vrubel, M. Bensimon, X. Hu, *Phys. Chem. Chem. Phys*, 2014, **16**,

5917-5921.

26. (a) A. E. Henkes, Y. Vasquez, R. E. Schaak, *J. Am. Chem. Soc*, 2007, **129**, 1896-1897. (b) J. Park, B. Koo, K. Y. Yoon, Y. Hwang, M. Kang, J. G. Park, T. Hyeon, *J. Am. Chem. Soc*, 2005, **127**, 8433-8440. (c) J. Wang, C. A. Johnston-Peck, J. B. Tracy, *Chem. Mater*, 2009, **21**, 4462-4467. (d) Y. Chen, H. She, X. Luo, G. H. Yue, D. L. Peng, *J. Cryst. Growth*, 2009, **311**, 1229-1233. (e) H. R. Seo, K. S. Cho, Y. K. Lee, *Mat. Sci. Eng. B*, 2011, **176**, 132-140.

27. (a) Y. Zhao, Y. P. Zhao, H. S. Feng, J. Y. Shen, *J. Mater. Chem*, 2011, **21**, 8137-8145. (b) J. Li, Y. Chai, B. Liu, Y. Wu, X. Li, Z. Tang, Y. Liu, C. Liu, *Appl. Catal. A: Gen*, 2014, **469**, 434-441.

28. G. S. Li, D. Q. Zhang, J. C. Yu, *Environ. Sci. Technol*, 2009, **43**, 7079-7085.

29. Y. Pan, R. R. Jia, J. C. Zhao, J. L. Liang, Y. Q. Liu, C. G. Liu, *Appl. Surf. Sci*, 2014, **316**, 276-285.

30. R. K. Chiang, R. T. Chiang, *Inorg. Chem*, 2007, **46**, 369-371.

31. D. Zhang, G. Li, J. C. Yu, *Cryst. Growth Des*, 2009, **9**, 2812-2815.

32. Y. Ni, L. Jin, J.Hong, *Nanoscale*, 2011, **3**, 196-200.

33. C. G. Morales-Guio, L. A. Stern, X. Hu, *Chem. Soc. Rev*, 2014, **43**, 6555-6569.

34. J. G. N. Thomas, *Trans. Faraday Soc*, 1961, **57**, 1603-1611.

35. B. E. Conway, B. V. Tilak, *Electrochim. Acta*, 2002, **47**, 3571-3594.

36. J. Yang, D. Voiry, S. Ahn, D. Kang, A. Kim, M. Chhowalla, H. Shin, *Angew. Chem. Int. Edit*, 2013, **52**, 13751-13754.

37. P. Xiao, Y. Yan, X., Ge, Z. Liu, J. Y. Wang, X. Wang, *Appl. Catal. B:*

*Environ*, 2014, **154**, 232-237.

38. C. X. Guo, L. Y. Zhang, J. Miao, J. Zhang, C. M. Li, *Adv. Energy Mater*, 2013, **3**, 167-171.

39. Y. Nicolet, A. L. de Lacey, X. Vernede, V. M. Fernandez, E. C. Hatchikian, J. C. Fontecilla-Camps, *J. Am. Chem. Soc*, 2001, **123**, 1596-1601.

40. A. D. Wilson, R. K. Shoemaker, A. Miedaner, J. T. Muckerman, D. L. DuBois, M. R. DuBois, *Proc. Natl. Acad. Sci. U. S. A*, 2007, **104**, 6951-6956.

41. (a) H. F. Du, Q. Liu, N. Y. Cheng, A. M. Asiri, X. P. Sun, C. M. Li, *J. Mater. Chem. A*, 2014, **2**, 14812-14816; (b) J. Q. Tian, Q. Liu, A. M. Asiri, X. P. Sun, *J. Am. Chem. Soc,* 2014, **136**, 7587-7590; (c) Z. H. Pu, Q. Liu, P. Jiang, A. M. Asiri, A. Y. Obaid, X. P. Sun, *Chem. Mater*, 2014, **26**, 4326-4329; (d) Q. Liu, J. Q. Tian, W. Cui, P. Jiang, N. Y. Cheng, A. M. Asiri, X. P. Sun, *Angew. Chem. Int. Ed,* 2014, **53**, 6710-6714.

42. (a) W. Cui, Q. Liu, Z. C. Xing, A. M. Asiri, K. A. Alamry, X. P. Sun, Appl. Catal. B, 2005, 164, 144-150; (b) Z. C. Xing, Q. Liu, A. M. Asiri, X. P. Sun, *Adv. Mater*, 2014, **26**, 5702-5707.

43. J. Q. Tian, Q. Liu, N. Y. Cheng, A. M. Asiri, X. P. Sun, *Angew. Chem. Int. Ed*, 2014, **53**, 9577 -9581.

44. Z. H. Pu, Q. Liu, C. Tang, A. M. Asiri, X. P. Sun, *Nanoscale*, 2014, **6**, 11031-11034.

45. P. Jiang, Q. Liu, X. P. Sun, *Nanoscale*, DOI: 10.1039/c4nr04866k.

46. P. Jiang, Q. Liu, Y. H. Liang, J. Q. Tian, A. M. Asiri, X. P. Sun, *Angew. Chem. Int. Ed,* 2014, **53**, 1-6.

47. (a) E. J. Popczun, J. R. McKone, C. G. Read, A. J. Biacchi, A. M. Wiltrout, N. S. Lewis, R. E. Schaak, *J. Am. Chem. Soc*, 2013, **135**, 9267-9270; (b) P. Liu, J. A. Rodriguez, *J. Am. Chem. Soc,* 2005, **127**, 14871-14878.

48. W. Zhang, J. Hong, J. Zheng, Z. Huang, J. Zhou, R. Xu, *J. Am. Chem. Soc*, 2011, 133, 20680-20683.

49. Q. Li, Z. C. Xing, A. M. Asiri, P. Jiang, X. P. Sun, *Int. J. Hydrogen Energ*, 2014, **39**, 16806-16811.

50. S. Gu, H. F. Du, A. M. Asiri, X. P. Sun, C. M. Li, *Phys. Chem. Chem. Phys*, 2014, **16**, 16909-16913.

# Figure Captions

**Fig. 1** XRD patterns of the as-synthesized nickel phosphide NCs at different P:Ni precursor ratios (a) P:Ni=0.65; (b) P:Ni=1.1; (c) P:Ni= 2.18; (d) P:Ni=5.45; (e) P:Ni= 7; (f) P:Ni=8.75.

**Fig. 2** TEM and HRTEM images of nickel phosphide NCs with different phases (a, b) $Ni_{12}P_5$, (c, d) $Ni_2P$, (e) $Ni_5P_4$. The size distribution and SAED pattern of $Ni_{12}P_5$ are inserted in images a and b. The size distribution and SAED pattern of $Ni_2P$ are inserted in images c and d. The SAED pattern of $Ni_5P_4$ is inserted in image e.

**Fig. 3** XPS spectra of the Ni 2p and P 2p regions for (a, b) $Ni_{12}P_5$, (c, d) $Ni_2P$ and (e, f) $Ni_5P_4$ NCs.

**Fig. 4** FT-IR analysis of the as-synthesized nickel phosphide NCs before (I) and after (II) annealing.

**Fig. 5** $N_2$ adsorption-desorption isotherms (a) and BJH pore-size distribution (b) of the as-synthesized nickel phosphide NCs with different phases.

**Fig. 6** Possible formation mechanism of the as-synthesized nickel phosphide NCs.

**Fig. 7** LSV curves of bare GCE, $Ni_{12}P_5$, $Ni_2P$ and $Ni_5P_4$ NCs in 0.5 M $H_2SO_4$.

**Fig. 8** Tafel plots of $Ni_{12}P_5$, $Ni_2P$ and $Ni_5P_4$ NCs.

**Fig. 9** (a) CV curves of $Ni_{12}P_5$, $Ni_2P$ and $Ni_5P_4$ NCs before (solid) and after (short dash) long-term 500 cycles. (b) Time-dependent current density curve of the $Ni_{12}P_5$, $Ni_2P$ and $Ni_5P_4$ NCs under static overpotential of 150 mV for 30 000 s.

**Fig. 10** Nyquist plots of $Ni_{12}P_5$, $Ni_2P$ and $Ni_5P_4$ NCs in 0.5 M $H_2SO_4$ with an overpotential of 200 mV. Inserted is an expansion of the high frequency region.

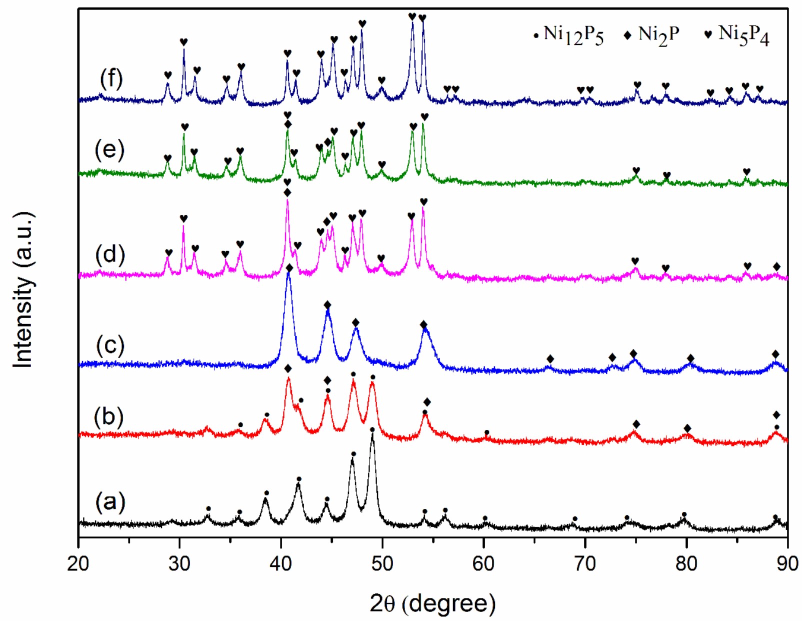


**Fig. 1** XRD patterns of the as-synthesized nickel phosphide NCs at different P:Ni precursor ratios (a) P:Ni=0.65; (b) P:Ni=1.1; (c) P:Ni= 2.18; (d) P:Ni=5.45; (e) P:Ni= 7; (f) P:Ni=8.75.

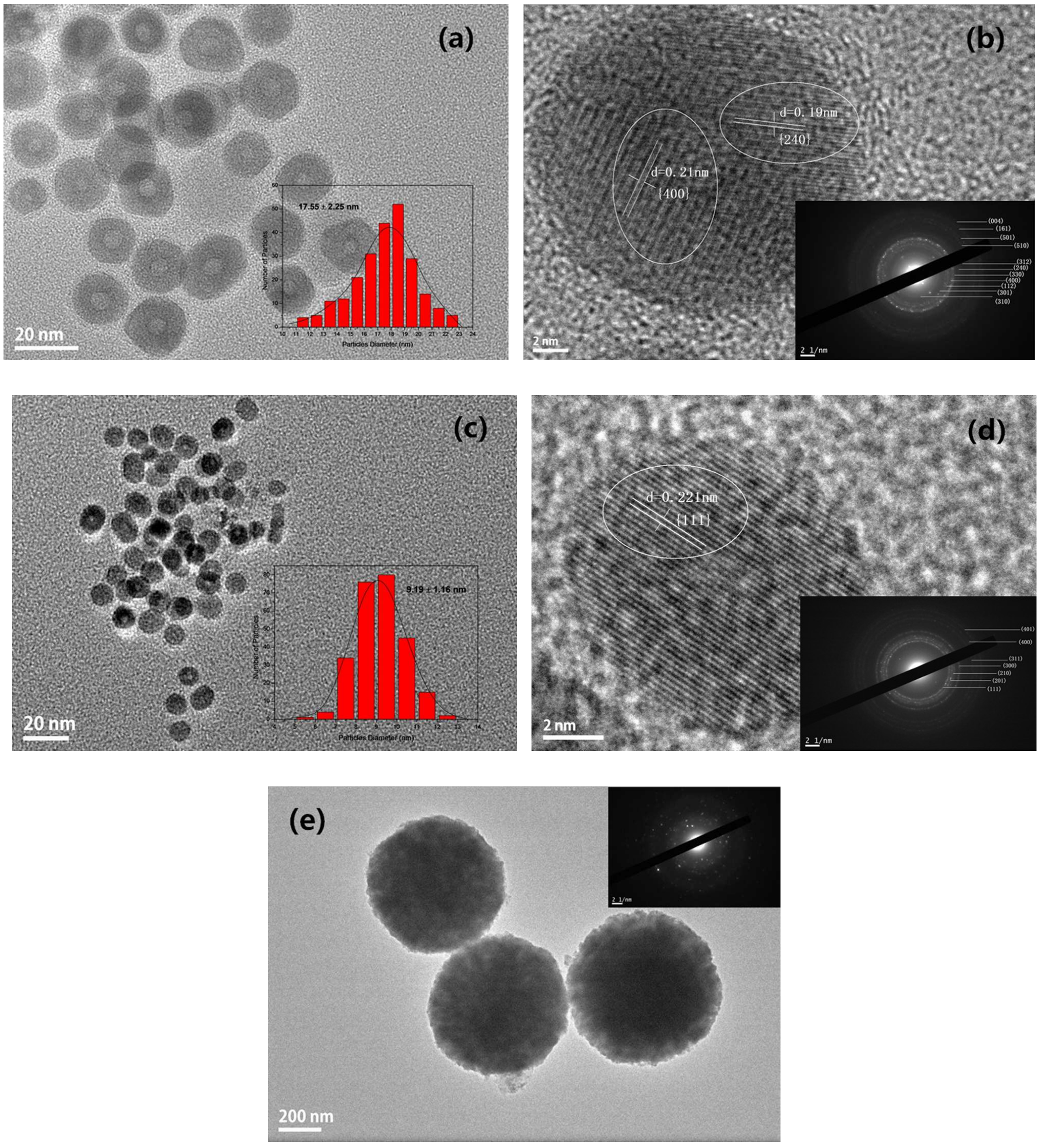


**Fig. 2** TEM and HRTEM images of nickel phosphide NCs with different phases (a, b) $Ni_{12}P_5$; (c, d) $Ni_2P$; (e) $Ni_5P_4$. The size distribution and SAED pattern of $Ni_{12}P_5$ are inserted in images a and b. The size distribution and SAED pattern of $Ni_2P$ are inserted in images c and d. The SAED pattern of $Ni_5P_4$ is inserted in image e.

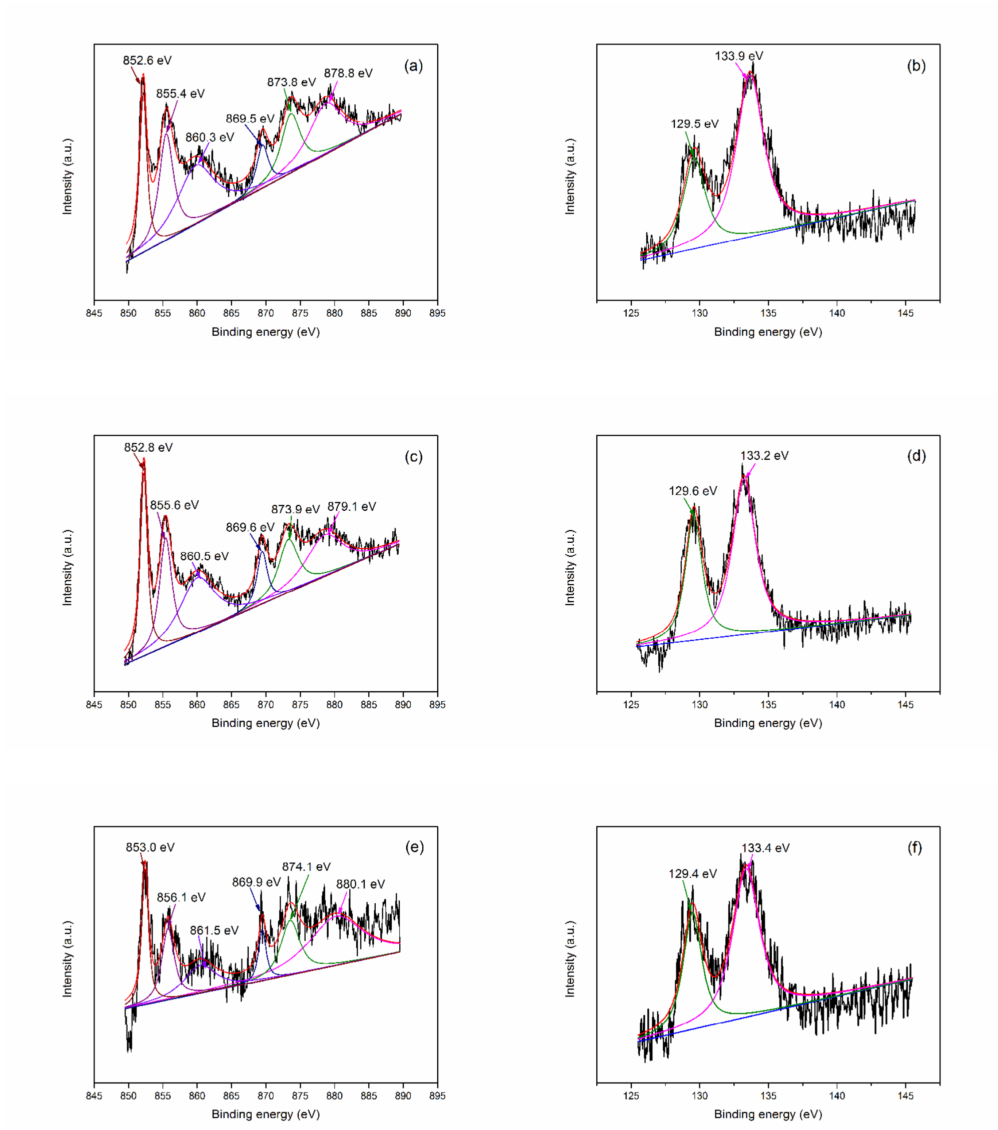


**Fig. 3** XPS spectra of the Ni 2p and P 2p regions for (a, b) $Ni_{12}P_5$, (c, d) $Ni_2P$ and (e, f) $Ni_5P_4$ NCs.

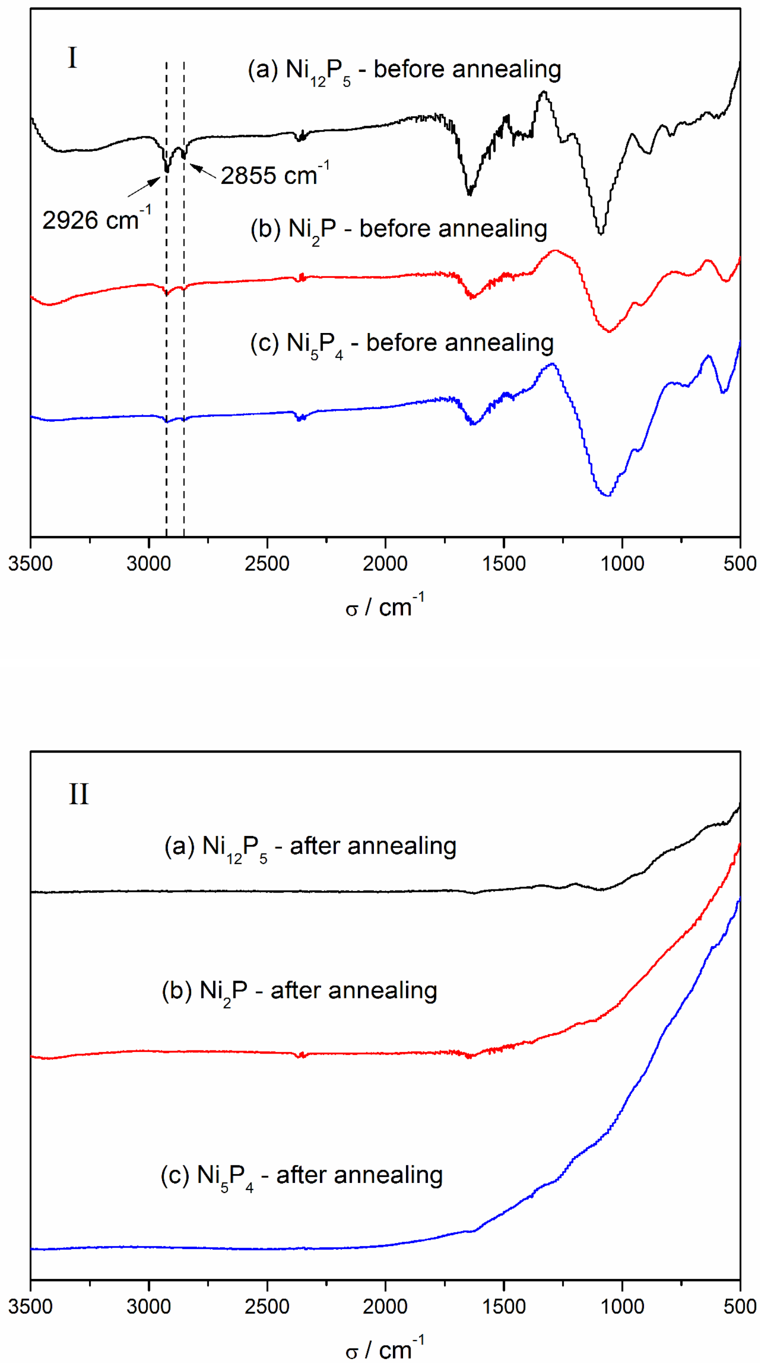


**Fig. 4** FT-IR analysis of the as-synthesized nickel phosphide NCs before (I) and after

(II) annealing.

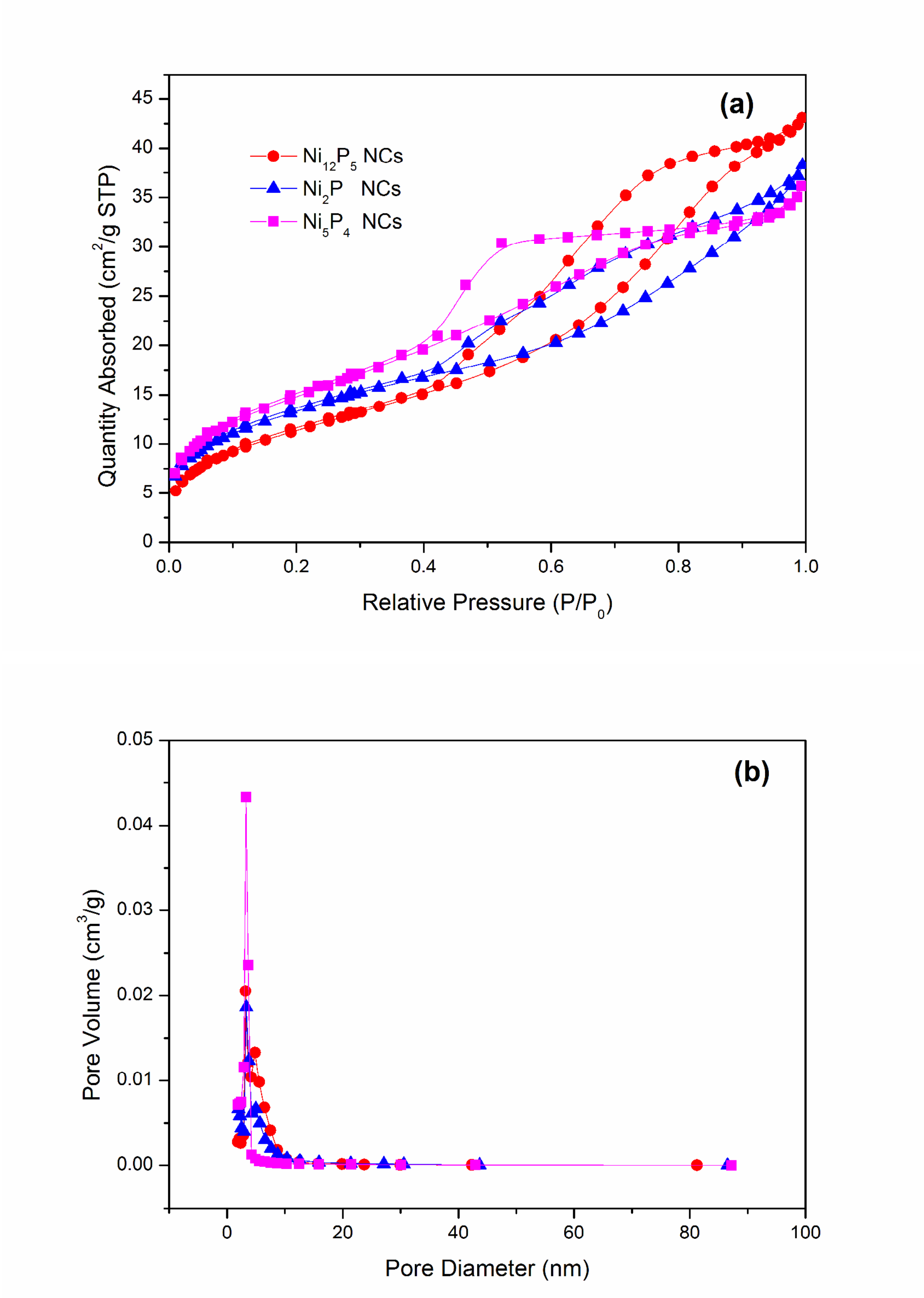


**Fig. 5** $N_2$ adsorption-desorption isotherms (a) and BJH pore-size distribution (b) of the as-synthesized nickel phosphide NCs with different phases.

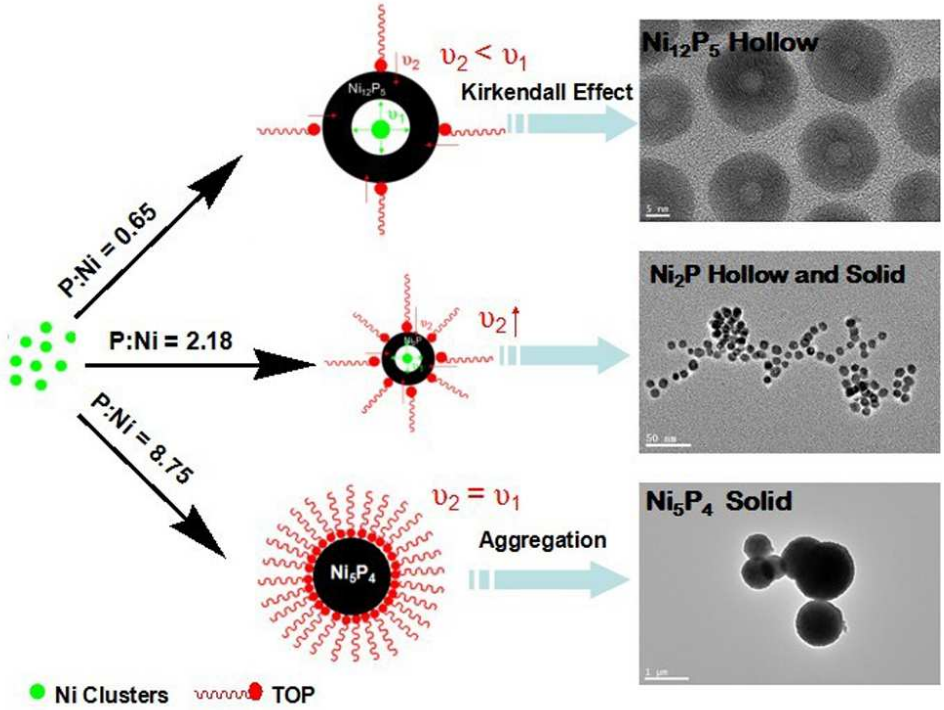


**Fig. 6** Possible formation mechanism of the as-synthesized nickel phosphide NCs with different phases and morphologies.

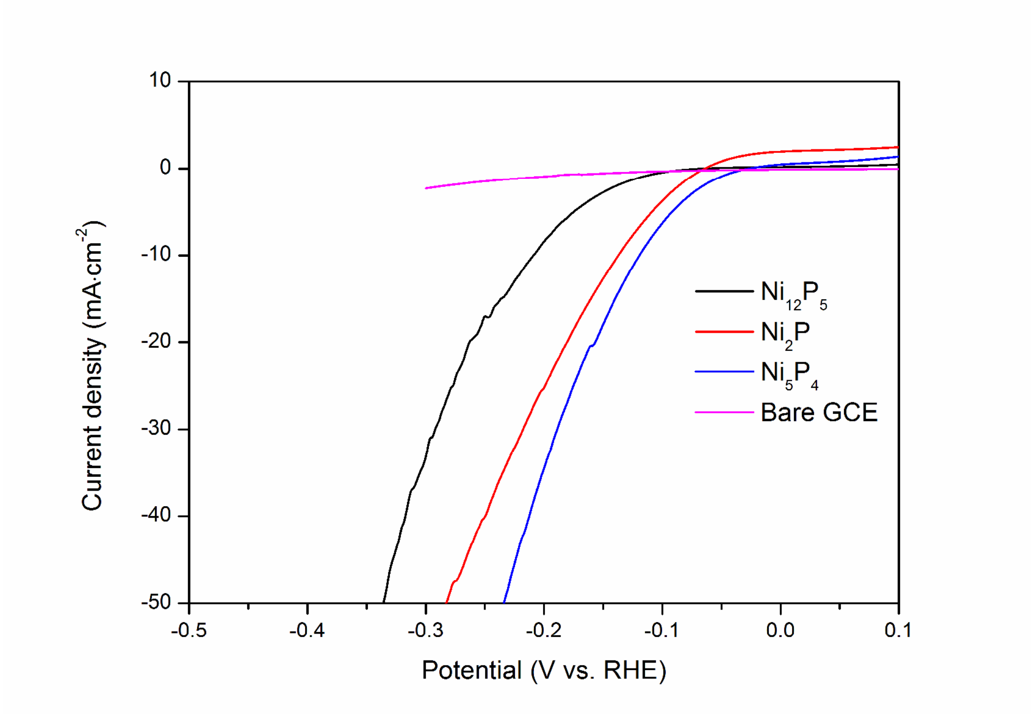


**Fig. 7** LSV curves of bare GCE, $Ni_{12}P_5$, $Ni_2P$ and $Ni_5P_4$ NCs in 0.5 M $H_2SO_4$.

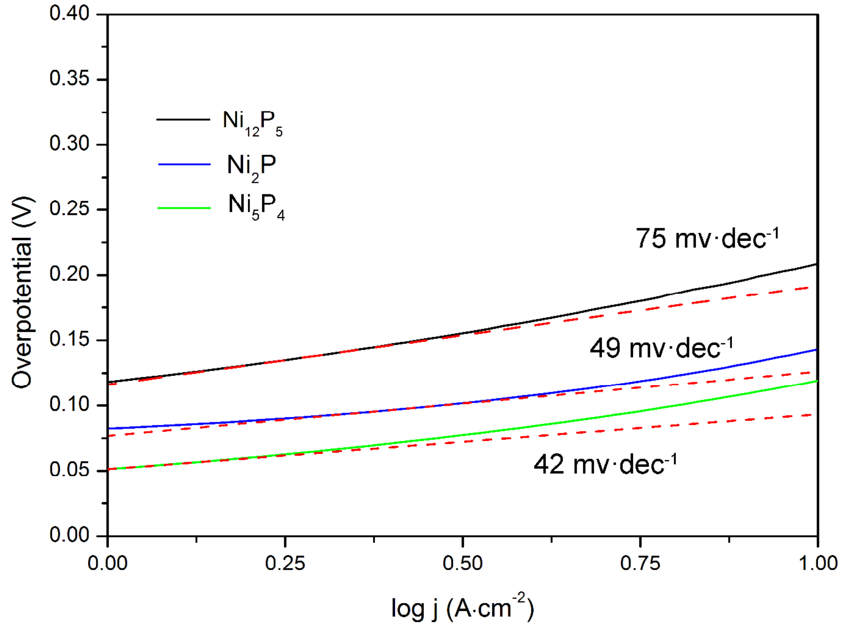


**Fig. 8** Tafel plots of $Ni_{12}P_5$, $Ni_2P$ and $Ni_5P_4$ NCs.

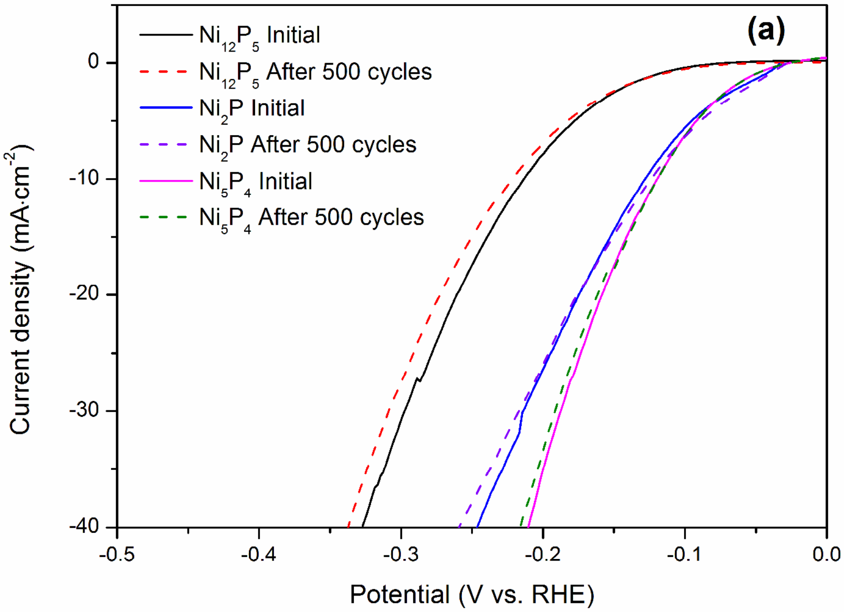


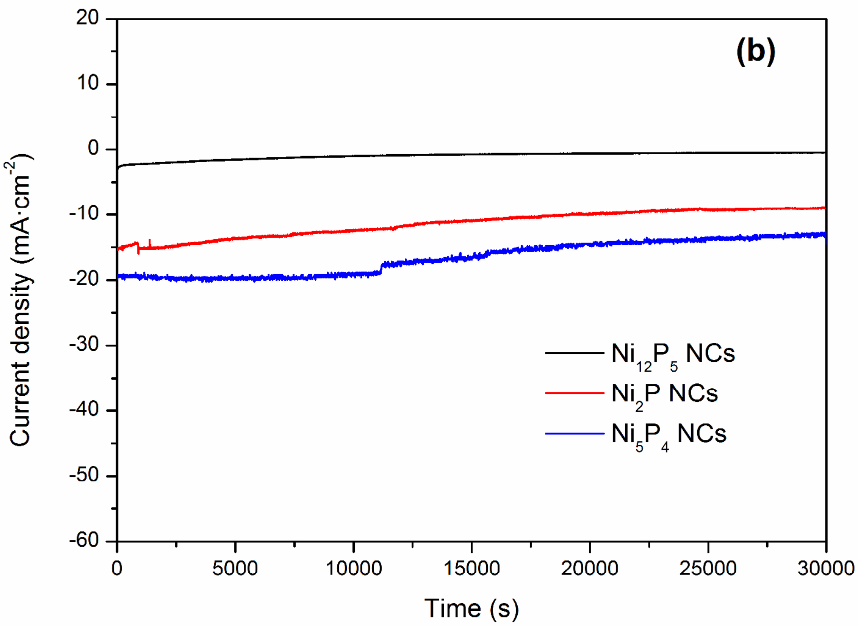


**Fig. 9** (a) CV curves of $Ni_{12}P_5$, $Ni_2P$ and $Ni_5P_4$ NCs before (solid) and after (short dash) long-term 500 cycles. (b) Time-dependent current density curve of the $Ni_{12}P_5$, $Ni_2P$ and $Ni_5P_4$ NCs under static overpotential of 150 mV for 30 000 s.

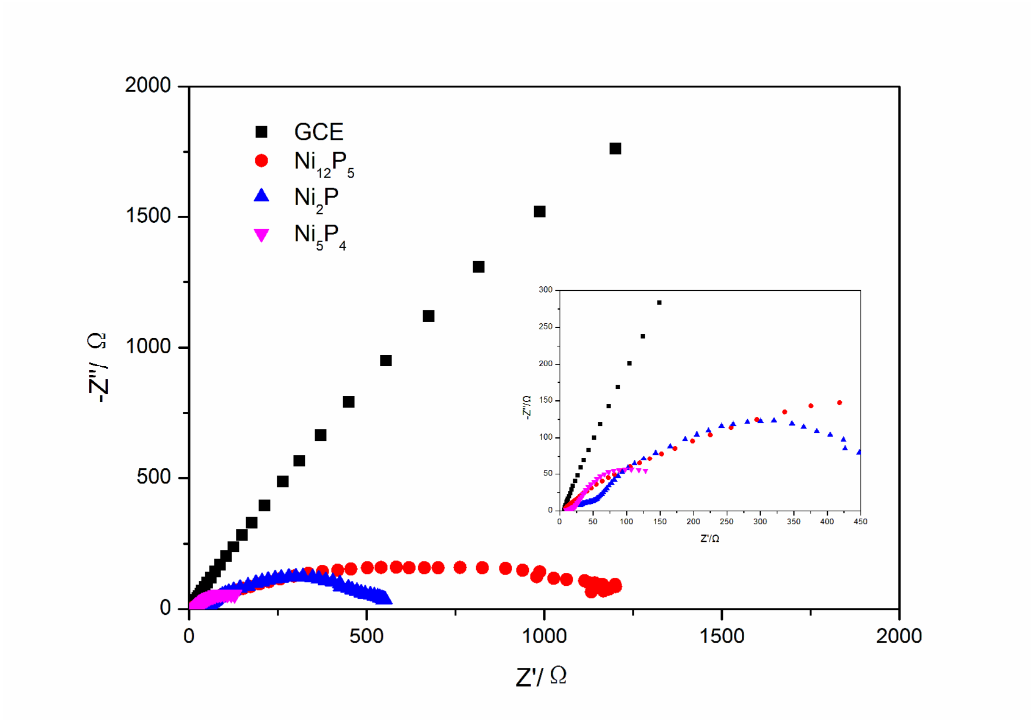


**Fig. 10** Nyquist plots of $Ni_{12}P_5$, $Ni_2P$ and $Ni_5P_4$ NCs in 0.5 M $H_2SO_4$ with an overpotential of 200 mV. Inserted is an expansion of the high frequency region.

Table 1 Textural properties of the as-synthesized nickel phosphide NCs with different phase.

| Catalyst | BET surface area ($m^2/g$) | Pore volume ($cm^3/g$) | Pore size (nm) |
|---|---|---|---|
| $Ni_{12}P_5$ | 42.2 | 0.06 | 6.22 |
| $Ni_2P$ | 48.4 | 0.05 | 4.76 |
| $Ni_5P_4$ | 54.2 | 0.04 | 4.01 |

# Graphic Abstract

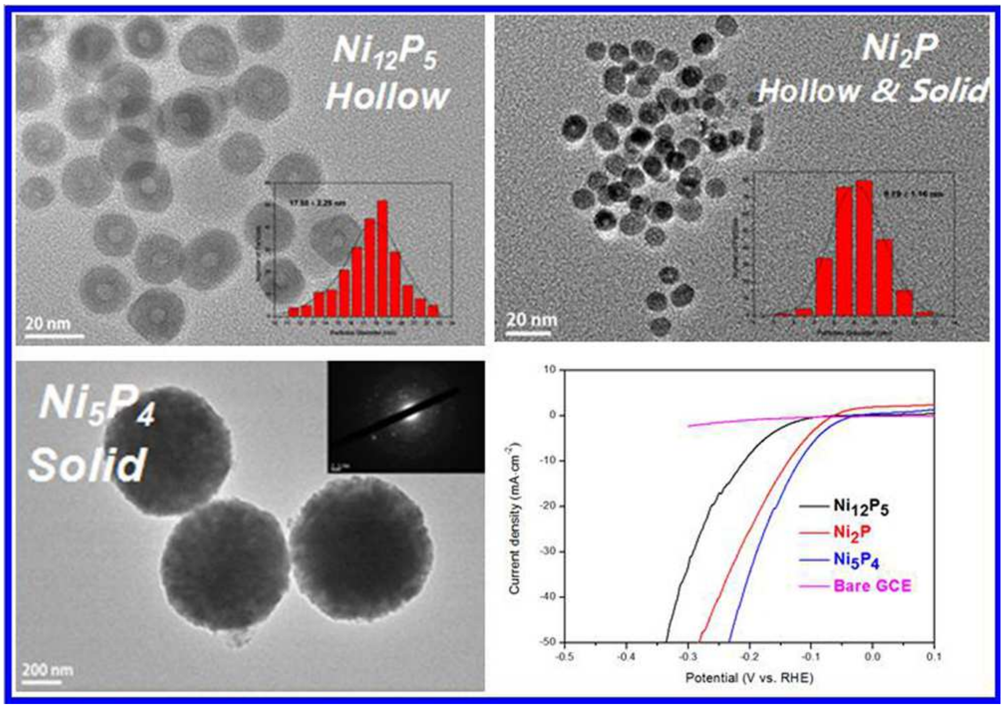


Monodispersed nickel phosphide NCs with different phases ($Ni_{12}P_5$, $Ni_2P$, $Ni_5P_4$) were successfully synthesized via the thermal decomposition approach. The phase influences of the nickel phosphide NCs on electrocatalytic properties for HER were investigated. The results showed that all phases of the as-synthesized nickel phosphide NCs have good catalytic properties, and that the $Ni_5P_4$ NCs with solid structure exhibited higher catalytic activity than the $Ni_{12}P_5$ and $Ni_2P$ NCs.